ELSEVIER

Journal of Power Sources 113 (2003) 255–270

JOURNAL OF POWER SOURCES

www.elsevier.com/locate/jpowsour

Strap grid tubular plate—a new positive plate for lead–acid batteries Processes of residual sulphation of the positive plate

D. Pavlov*, G. Papazov, B. Monahov

Central Laboratory of Electrochemical Power Sources, Bulgarian Academy of Sciences, Acad. G. Bonchev Street bl.10, 1113 Sofia, Bulgaria

Abstract

For almost a century now the tubular plate design has been based on cylindrical tubes and spines. The contact surface between the positive active mass (PAM) and the spine is small, which results in high polarisation of the plate at high discharge currents and low power output of the cell. In an attempt to eliminate these disadvantages, the shape of the tubes has been changed to flattened elliptic and the spines have been replaced by strap grids. The thickness of this new type of tubular plate, strap grid tubular plate (SGTP), is between 3 and 5 mm. Batteries with tubular plates of the new design (SGTP batteries) can be used in electric vehicle (EV) and photovoltaic (PV) system applications. This paper presents results of SGTP battery tests according to the European standards for EV, hybrid electric vehicle (HEV) and photovoltaic (PV) system batteries. SGTP batteries have a cycle life of 1000 ECE-15-EV cycles, 6000 ECE-HEV cycles and more than eight gross PV cycles. The optimum battery charge algorithm for VRLA batteries with strap grid tubular plates has been established and the mechanism of disintegration of the positive active mass has been disclosed. The following phenomena are responsible for the decline in capacity of the positive plates. First, when the PAM is built up of globules adhering closely to each other, a strong skeleton with thick aggregates (branches) *with a membrane surface* is formed. The surface layer of the branches impedes the access of H_2O and H_2SO_4 to their interior thus reducing the utilisation of the PAM. Besides, internal stresses are created in the aggregates, which cause them to crack. Secondly, when the PAM is built up of individual agglomerates with micropores in between, a porous mass with large surface is formed. The tubes keep the aggregates together and prolong the cycle life of the battery. During discharge, the contacts between the aggregates weaken and the capacity declines. Third, during discharge, the H_2SO_4 concentration in the pores of the plate inner layers (close to the straps) increases. In concentrated H_2SO_4 solution the solubility of $PbSO_4$ crystals decreases. This slows down the rate of oxidation of $PbSO_4$ to PbO_2. Some parts of the $PbSO_4$ crystals in the PAM of the charged plate remain unoxidised (residual sulphation). Thus, the capacity of the plate is lower. Strap corrosion is the phenomenon that may limit the cycle life of SGT plates.

Keywords: Lead–acid battery; Tubular lead dioxide plates; Structure of lead dioxide active mass; Electric vehicle batteries; Photovoltaic batteries

1. Introduction

On battery cycling, the active materials of the positive and negative plates expand during discharge and shrink during charge [1]. The amplitudes of these pulsations vary with the number of cycles due to changes that occur in the structure of the active masses and in the pore volume. These changes are illustrated in Fig. 1.

After a certain number of cycles, the negative plates start to lose porosity because of degradation of the expander in them, and consequently the capacity of the plates starts to decline.

The thickness of the positive active mass (PAM) increases on cycling until the PAM begins to shed. The PAM expansion leads to a loss of contact between the PAM and the grid as well as between the individual PAM aggregates, which also results in capacity decline. This process often limits the cycle life of the battery. In order to avoid these adverse effects, PAM expansion should be limited.

There are two basic methods to restrict expansion of the positive plates. The first one is by applying external pressure to the active block (25–30% compression). Absorptive glass mat (AGM) or glass mat (GM) separators are used in this case [2]. Through active block compression the volume within which the PAM can expand is limited. However, this method causes the AGM separator to contract, the quantity of electrolyte between the plates to decrease and the negative plates to shrink.

The second widely used method is to enclose the PAM into tubes (gauntlets). In this case, the positive active mass expands within a restricted volume only. The role of active block compression is not critical. However, the tubular

* Corresponding author. Tel.: +359-2-71-8651; fax: +359-2-73-1552.
E-mail address: dpavlov@mbox.cit.bg (D. Pavlov).

0378-7753/02/$ – see front matter
PII: S0378-7753(02)00521-9

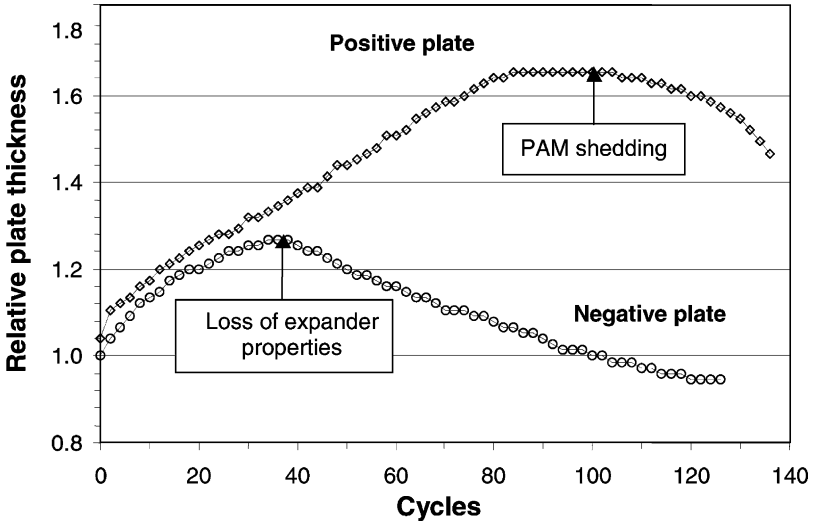

Fig. 1. Relative plate thickness changes during cycling.

plates are thick and the batteries produced using such plates have low charge acceptance, satisfactory specific energy and long cycle life, but low power output.

The aim of the present work is to find out whether it is possible to improve the power output and charge acceptance of tubular plates through the use of a new design, and thus make them suitable for electric vehicle and photovoltaic battery applications.

2. Experimental

2.1. Strap grid tubular plate design

The tubular plate design is usually based on cylindrical tubes (Fig. 2a) with a diameter of about 8.4 mm. A thick layer of active mass is formed in the tubes and the contact surface between PAM and the spine is small. $\gamma = 2.0$–2.4 g PAM/cm^2 of spine surface. This tubular plate design results in high polarisation of the plate at high current discharge and low power output.

In an attempt to eliminate the described shortcomings, the shape of the tubes has been changed from cylindrical to flattened elliptic (Fig. 2b) and the current collector spines have been replaced with strap grids [3]. This new plate design has the following advantages: lower coefficient $\gamma = 0.8-0.9$ g PAM/cm^2 of strap surface, smaller thickness of the SGT plate (between 3.0 and 5.0 mm) and reduced PAM thickness (down to 1.0 mm).

Two types of SGT plates have been developed based on two different strap grid technologies:

(a) Cast strap grids with a thickness of 1.2–1.5 mm. The plates have a thickness of 4 or 5 mm.

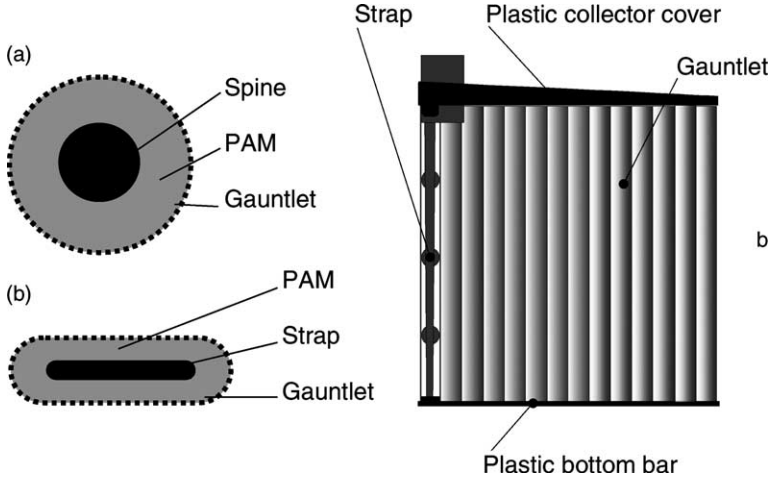

Fig. 2. Tubular and strap grid tubular plates designs.

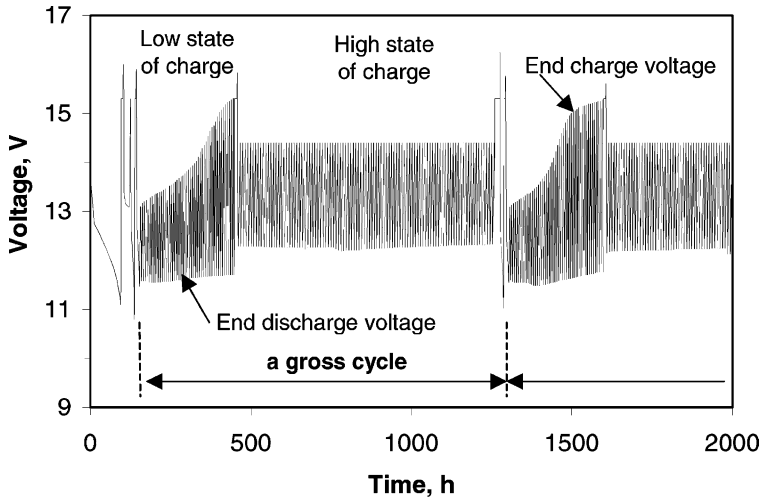

Fig. 3. Voltage changes during cycling [4].

(b) Die-cut strap grids with a thickness of 1.0–0.9 mm. The plates are 3.0–4.0 mm thick.

Both types of strap grids are produced using PbSnCa alloys.

2.2. Strap grid tubular plate preparation

First, 4BS paste was prepared at a temperature of 90 °C. The 4BS paste was diluted with water to a suspension with a density of 1.80 g/cm^3.

Die-cut or cast strap grids were inserted into the flattened elliptic (or rectangular) gauntlets. The tubes were filled with the 4BS suspension under pressure. The density of the paste in the tubes was 4.6 g/cm^3 and the ratio PAM weight/die-cut strap grid weight was 1.50. The tubular plates thus produced were set to curing. The cured plates were assembled into cells with three positive and four negative plates and AGM separators between them. These active blocks were introduced into batteries under 10 or 20% compression. The batteries were set to a standard formation process.

2.2.1. Battery test procedure

2.2.1.1. Photovoltaic batteries. The IEC 61427 standard [4] for testing of photovoltaic batteries includes battery cycling at low state of charge (90% DOD) for 50 cycles followed by cycling at high state of charge (25% DOD) for another 100 cycles. These 150 cycles form a gross cycle with an overall duration of 1100 h. Then the capacity (C_{10}) is measured and cycling continues at low and then at high state of charge

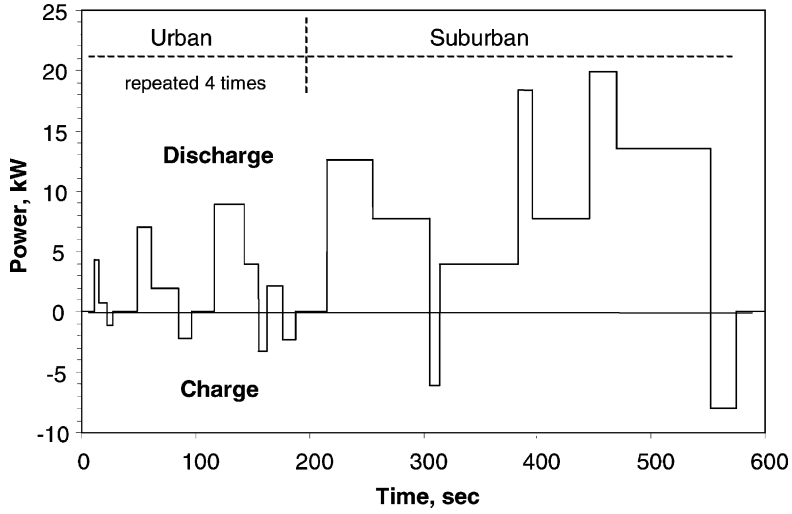

Fig. 4. ECE-15 cycling test profile [5].

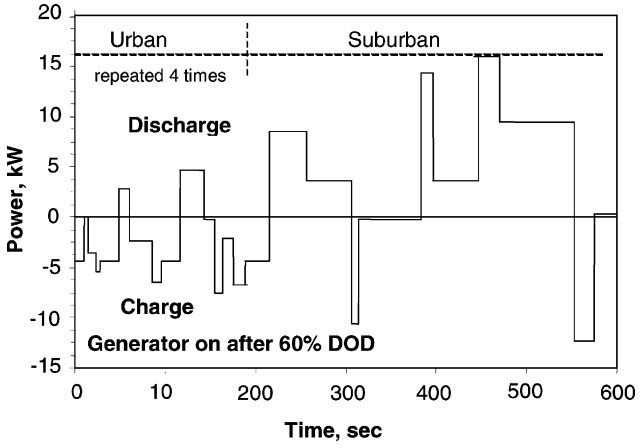

Fig. 5. ECE-15-HEV power profile [6].

again. Fig. 3 shows the changes in battery voltage on cycling according to the above standard.

2.2.1.2. Electric vehicle batteries. The ECE-15 test algorithm [5] for electric vehicle batteries is presented in Fig. 4. It is based on a standard European test cycle, speed versus time, and the battery power profile is calculated using a EUCAR reference electric vehicle.

Each cycle consists of two parts, one urban part which is repeated four times without rest periods, followed by one suburban part. The overall cycle is 1180 s long and is repeated without rest periods until the end of discharge is reached. The end of life criterion is when the battery fails to deliver 80% of its useful capacity, which is the average capacity of the first three ECE cycles.

2.2.1.3. Hybrid electric vehicle batteries. With the introduction of hybrid electric vehicles in 1997, the ECE-15 cycling test was modified with the ECE-15-HEV algorithm [6]. Fig. 5 shows the changes in power output on ECE-15-HEV cycling.

According to this standard, during the first three cycles the car generator is off and the battery is discharged (Fig. 6).

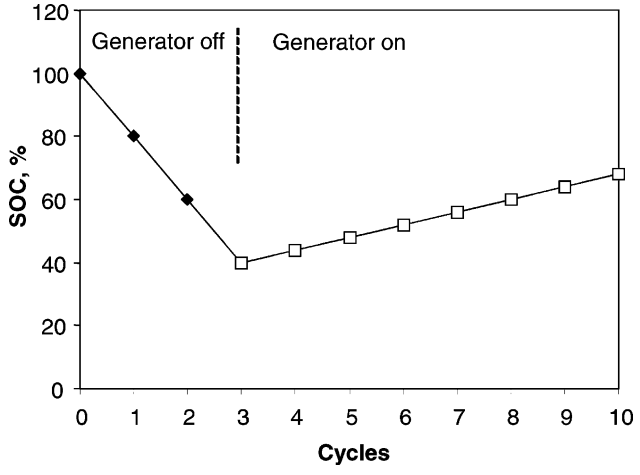

Fig. 6. State of charge during the high power life cycle test [6].

When the battery reaches 60% DOD, the engine (and the generator) is started and it operates in parallel with the battery. An additional charge current is added to the ECE discharge and charge pulses. During the next seven HEV cycles the battery and the engine operate in parallel. As a result of this additional charge the battery will be charged with about 4% per cycle. After every 10 cycles, the battery is subjected to a full charge (Fig. 6).

3. Experimental results and discussion

3.1. Influence of strap surface on the formation of groups of $PbSO_4$ crystals at the grid/PAM interface

It has been established that on deep cycling of tubular positive plates with die-cut strap grids, a rapid capacity loss is observed in some of the cells (PCL-1). This phenomenon has not been observed with cast strap grid tubular plates when PbSnCa alloy is used, i.e. an alloy similar to that of the die-cut grids. *Hence, it is the method of grid manufacture, and particularly the flatness (smoothness) of the strap grid surface, that affects the cycle life of the cells*. SEM observations of the PAM/grid interface evidence the formation of numerous groups of $PbSO_4$ crystals located between the corrosion layer and the PAM. SEM micrographs of these groups of $PbSO_4$ crystals are presented in Fig. 7.

The smooth die-cut strap surface facilitates the formation of a uniform pore system and a uniform skeleton in the PAM/strap interface. During discharge, the reduction of PbO_2 proceeds at a uniform rate in the interface layer and plate-like $PbSO_4$ crystals are formed over the surface of the corrosion layer. This is the reaction layer where the flow of Pb^{2+} ions, released by the reduction of PbO_2, meets the flow of H_2SO_4 coming from the bulk of the solution. As the oversaturation with Pb^{2+} and SO_4^{2-} ions occurs in a thin layer of pores, plate-like $PbSO_4$ crystals are formed in this layer. These crystals block the pores. The $PbSO_4$ crystals cannot be fully oxidised to PbO_2 during the next charge cycle. Then during the next discharge, the same processes take place. Thus, groups of $PbSO_4$ "roses" are formed (Fig. 7). The contact area between PAM and the strap is reduced and the capacity declines.To prevent the formation of groups of interconnected $PbSO_4$ crystals, the surface of the straps should be made rough.

Roughening of the metal surface can be achieved by various techniques, for example:

(a) through mechanical treatment of the strap surface;
(b) through subjecting the battery to reverse polarisation before formation proper. As a result of this procedure, Pb is deposited here and there on the smooth metal surface thus making the surface of the strap grid rough. After this treatment the PCL-1 effect does not appear.

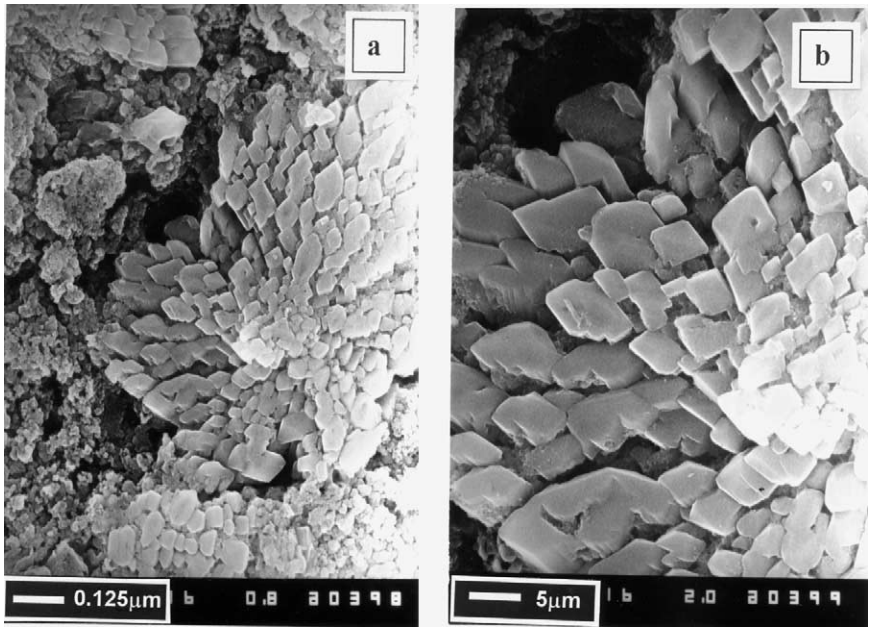

Fig. 7. SEM micrographs of a region in the corrosion layer/PAM interface containing $PbSO_4$ crystals.

3.2. PV battery test results

The batteries in photovoltaic energy systems operate mostly at partial state of charge. This operation mode facilitates the processes of sulphation and recrystallisation of $PbSO_4$ to proceed in both active masses. These processes strongly influence the cycle life of the batteries.

Fig. 8 presents the results of the SGTP battery tests performed according to the PV batteries test protocol. As is evident from the figure, the battery with SGT plates has stable voltage performance throughout the low state of charge cycles. These results indicate that the batteries have good charge acceptance and high power performance on cycling at partial state of charge. Up to now, the batteries have undergone eight gross cycles or 8800 h. The tests are going on. For comparison, batteries with expanded grids and pasted plates have a cycle life of two to three gross cycles or 2200–3300 h.

3.3. ECE-15-EV test results

A battery with die-cut strap grids was used for this test. The tubular plates were 3 mm thick. The battery was charged employing the *IU* algorithm ($I = 0.4C$ A, $U = 15.0$ V, charge

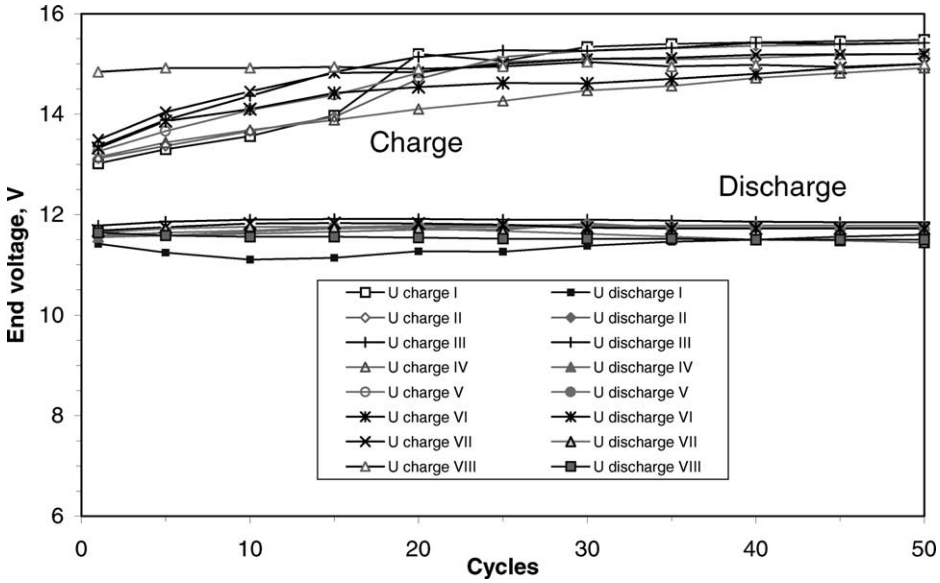

Fig. 8. End-of-charge and end-of-discharge voltage on PV battery cycling at low state of change (90% DOD) for eight gross cycles.

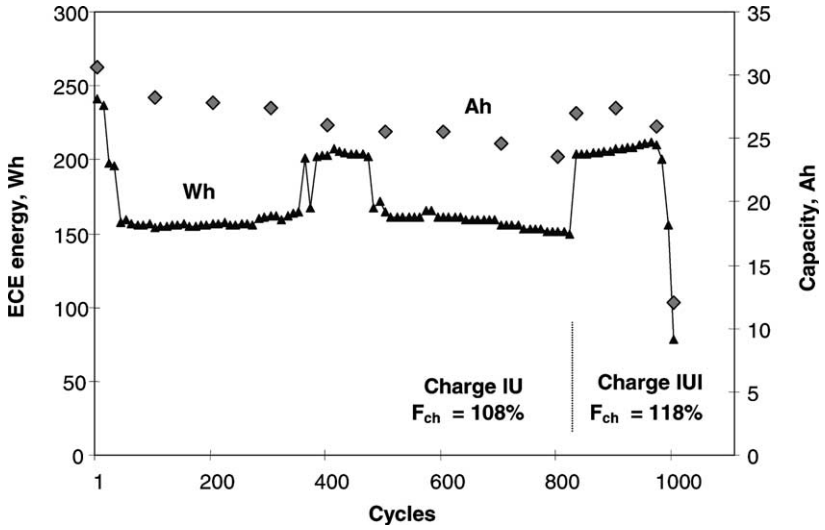

Fig. 9. Capacity and ECE energy output during cycling of a SGTP battery according to the ECE-15-EV test procedure.

factor $F_{ch} = 108\%$) for 850 cycles followed by $I_1U_2I_3$ charge algorithm ($I_1 = 1.5C$ A, $U_2 = 15.2$ V to $F_{ch} = 108\%$; $I_3 = 0.1C$ A to $F_{ch} = 118\%$). The capacity and energy output of the SGTP battery on cycling following the ECE-15 test profile are presented in Fig. 9.

On cycling with a charging current $I = 0.4C$ A to $F_{ch} = 108\%$, a decrease in energy output from 250 to 160 W h was observed. On further cycling employing the second charge algorithm, i.e. current $I_1 = 1.5C$ A and $F_{ch} = 118\%$, the energy output increased to 200–250 W h despite the 800 cycles that the battery had undergone. Only after 990 cycles, the health of the battery declined abruptly and it reached its end of life after 1000 cycles due to deep inter-crystalline corrosion in several strap grids and considerable softening of the PAM in some of the tubes.

Fig. 9 illustrates also the changes in C_2 capacity (measured after every 100 ECE cycles) as a function of the number of cycles. The cycle life of about 1000 charge/discharge cycles under these conditions corresponds to an EV distance run of about 50,000 km. For comparison, EV batteries with 1 mm thick expanded grid plates have exhibited a maximum cycle life of 100 cycles on ECE-15-EV testing.

The observed increase in battery capacity and energy output after switching to the second charge algorithm indicates that the full energy capacity of the battery may be extracted through optimisation of the charge regime.

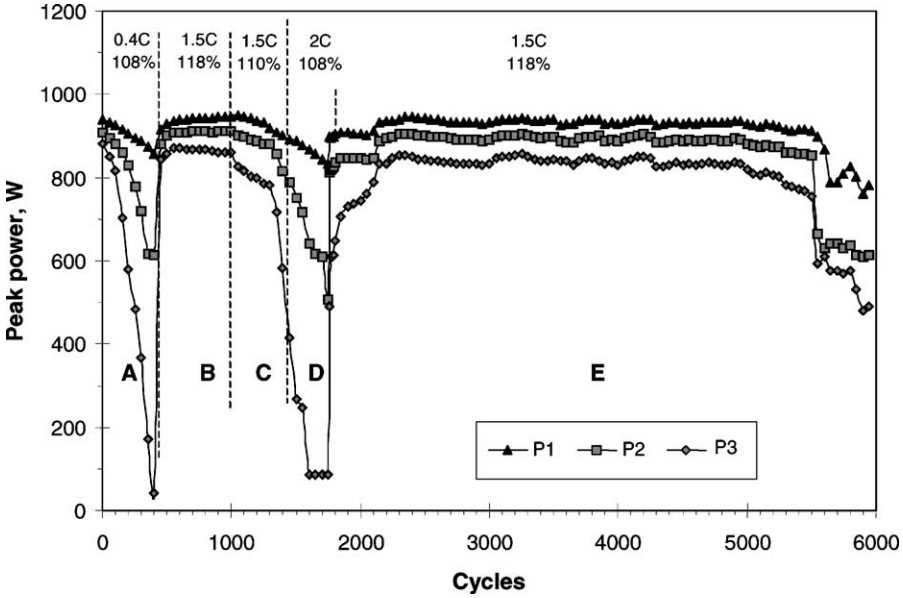

Fig. 10. Peak power changes during cycling of a SGTP battery for hybrid electric vehicle applications.

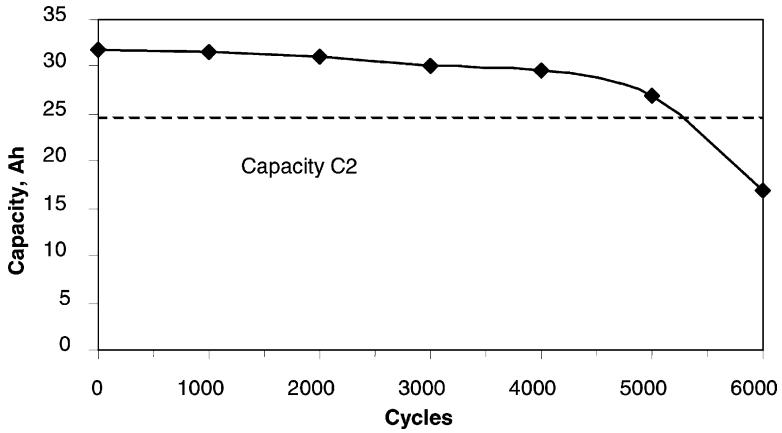

Fig. 11. Capacity (C_2) changes on battery cycling according to the ECE-15-HEV test algorithm.

3.4. Hybrid electric vehicle test results

During the cycling test the peak power in the first three ECE cycles was measured before the charge generator was switched on. Fig. 10 presents the peak power values as a function of the number of cycles. P_1 denotes the power delivered at the maximum discharge current during the first ECE cycle, P_2 the power output during the second ECE cycle and P_3 during the third ECE cycle prior to switching on the generator.

In the region marked with A (Fig. 10), I_1 and F_{ch} are below their optimum values and hence the power output of the battery decreases on cycling. In the regions marked with C and D, the charging current I_1 is above its optimum value ($I = 1.5C$ A) and the charge factor is lower than the optimum one. The peak power P_3 decreases with cycling. When in the regions marked with B and E the charge factor reaches its optimum value ($F_{ch} \approx 118\%$), the power output increases and this higher value is preserved for more than 4000 cycles (region E). This fairly high charge factor $F_{ch} \cong 118\%$ leads to increased water loss. The cells need topping up with water (25 ml per cell) after every 1000 ECE-HEV cycles.

The results presented in Fig. 10 evidence a battery life of 5500 hybrid cycles, which corresponds to a distance run of about 55,000 km.

The changes in battery capacity C_2 (2 h rate of discharge), measured after every 1000 cycles, are presented in Fig. 11. It can be seen from the figure that, under these charge conditions, the capacity of the battery remains almost constant for more than 5000 ECE-HEV cycles and decreases thereafter leading to end of battery life.

Fig. 12 illustrates the changes in internal resistance of the battery cells, measured at high current (165 A) at different DOD. The data in the figure indicate the internal resistance of the fully charged (0% DOD) battery increases from 3.8 mΩ per cell during the first cycle to 6.1 mΩ per cell after 6000 cycles. These changes in behaviour of the internal resistance on discharge are related to changes in the structure of the active mass and of the interface of the PAM with the strap.

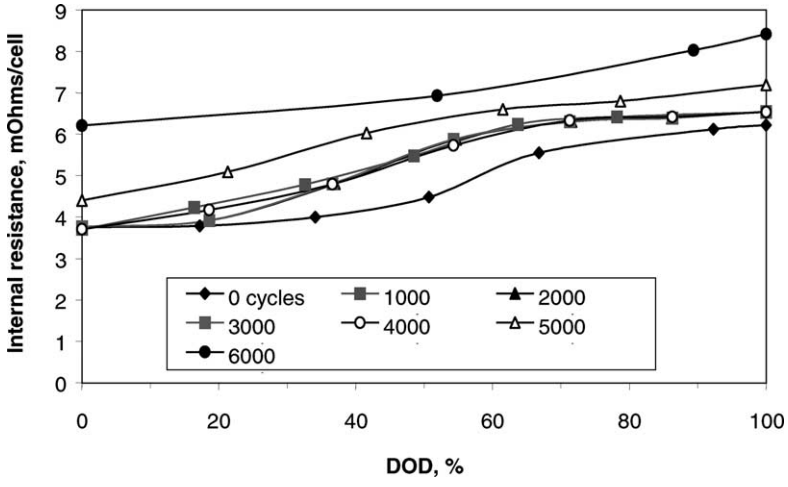

Fig. 12. Internal resistance of the battery at different DOD.

3.5. Degradation of the PAM structure in SGTP on cycling of VRLA batteries according to the ECE-15 test procedure

3.5.1. Changes in the pore system on cycling

An integral PAM sample was taken from different sites of the SGT plate and set to Hg porosimetry to determine the pore volume distribution by radius. Such measurements were performed after 1, 100, 200 and 380 cycles. After 600 cycles, the PAM becomes soft at many places and hence the porosimetric determinations are incorrect. However, the data obtained by the pore volume measurements until the 380th cycle provide sufficient information about the phenomena proceeding on PAM cycling.

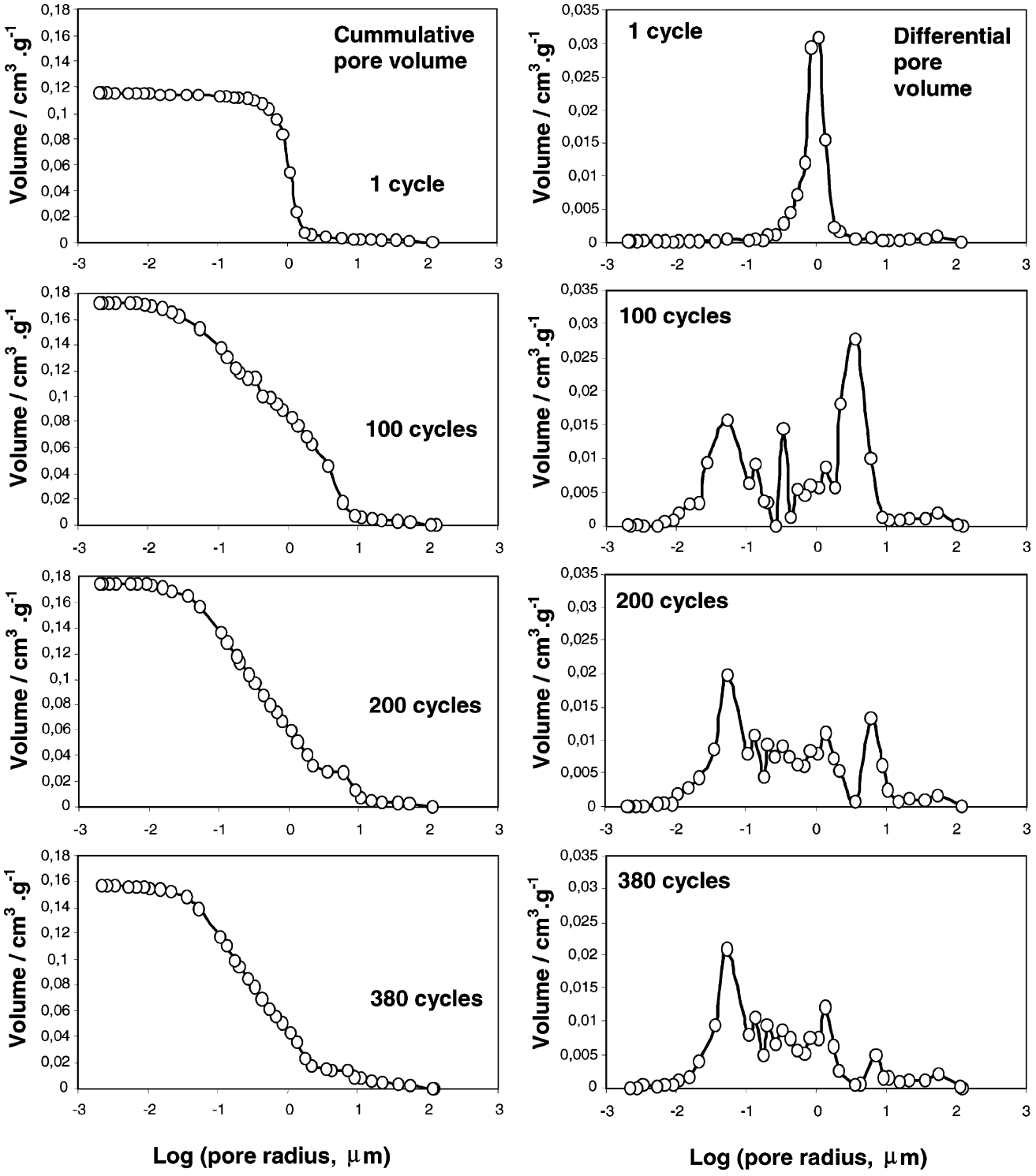

Fig. 13. Cumulative and differential pore volume as a function of pore radius for PAM samples after 1, 100, 200 and 380 cycles.

Fig. 13 illustrates the changes in cumulative and differential pore volume as a function of pore radius. After plate formation (first cycle), the cumulative pore volume is 0.12 cm^3/g PAM, which increases to 0.17 cm^3/g on cycling and remains constant as it is limited by the gauntlets' volume. The pore volume distribution by radius changes but within the same pore volume of PAM. Fig. 13 shows that after formation the PAM contains mainly macropores with radii of about 1 μm. For about 100 cycles, macropores with radii ranging between 5 and 10 μm are formed. Considerable amounts of micropores (0.1–0.04 μm) are also detected as well as pores of medium size with radii ranging from 2–3 μm to 0.1 μm. On further cycling, the share of macropores decreases, whereas that of the medium sized pores increases.

If this tendency is considered from the point of view of the PAM structure, it indicates that at the beginning of cycling a skeleton of large aggregates (branches) is formed. On further cycling, the skeleton structure disintegrates, whereby the aggregates fall apart to smaller aggregates and agglomerates, which are responsible for the pores with radii between 0.1 and 2 μm. The decrease in average pore radius slows down the movement of the H_2SO_4 flow along the pores in the inner parts of the PAM. The above results show that, when the battery operates under pulse charge/discharge mode or at partial state of charge, the structure of PAM disintegrates very quickly (for about 200 cycles). Thanks to the tubular plate design, the dispersed PAM is kept together within the region of densities higher than the critical value ($d = 3.60$ g/cm^3 PAM) [7]. PAM can accumulate and generate current. Therefore, the strap grid tubular plate design is very suitable for pulse charge/discharge mode operation.

3.5.2. Phase composition of PAM and of the corrosion layer after 380 cycles

The changes in phase composition through the cross-sections of tubular plates after 380 cycles were examined. Samples were taken from the corrosion layer (CL), the AMC Layer and the PAM at various distances from the strap surface, and these were X-rayed. AMCL means the layer of PAM connecting PAM with the CL (active mass connecting/contacting/layer—AMCL) [3]. Fig. 14 illustrates the changes in the content of β- and α-PbO_2, and of $PbSO_4$ in fully charged plates.

The active mass of a fully charged plate contains mainly β-PbO_2. The latter's amount is the greatest close to the tube surface. β-PbO_2 is also found in the CL. The α-PbO_2 modification is detected mainly in the CL and in the AMCL. As the characteristic diffraction line for α-PbO_2 ($d = 0.311$ nm) coincides with that for tet-PbO, the intensity of this line may be due also to the presence of tet-PbO obtained as a result of the oxidation of lead.

Fig. 14 shows that the intensity of the β-PbO_2 line (i.e. the amount of β-PbO_2 crystals) in the inner PAM layer decreases almost two times as compared to that on the plate surface.

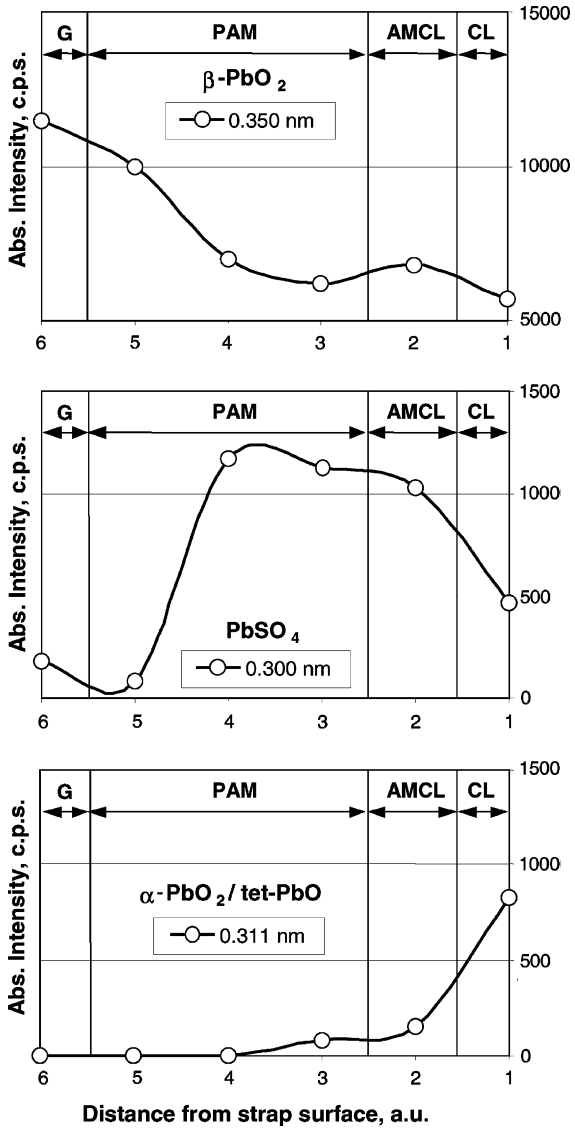

Fig. 14. Changes in phase composition (β-PbO_2, $PbSO_4$ and α-PbO_2) of PAM as a function of distance from the strap surface.

This, however, does not lead to an equivalent increase in the amount of α-PbO_2. Indeed, the $PbSO_4$ content in the PAM and AMCL layers increases, but this increase, too, is not equivalent to the decrease of the β-PbO_2 content. Most probably, part of the PbO_2 in the PAM and AMCL layers is hydrated and becomes amorphous [8].

3.5.3. Mechanism of the processes of residual sulphation in the interior of the positive plates

Fig. 14 indicates that both the PAM and AMCL layers contain $PbSO_4$ although the plates are fully charged. There must be some reasons for the impeded oxidation of $PbSO_4$ to PbO_2. During charge, H_2SO_4 is formed in the pores of PAM as a result of the $PbSO_4$ oxidation to PbO_2

$$PbSO_4 + 2H_2O \rightarrow PbO_2 + H_2SO_4 + 2e^- + 2H^+$$

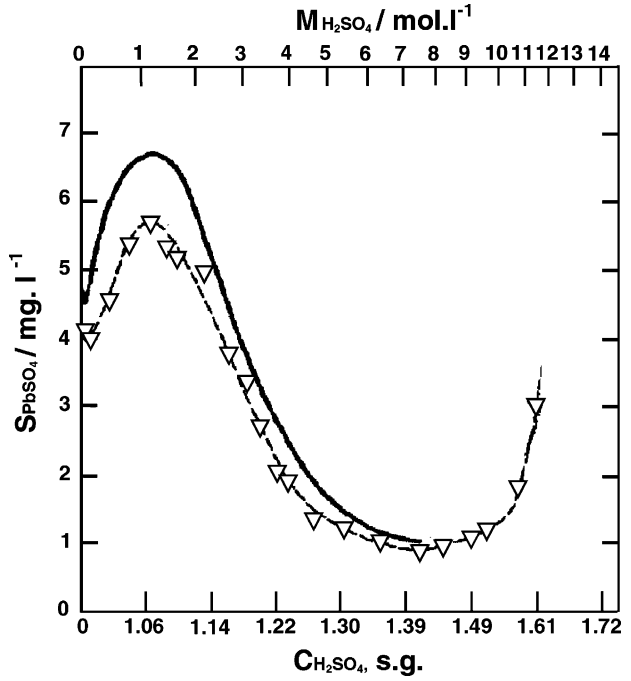

Fig. 15. Dependence of $PbSO_4$ solubility on H_2SO_4 concentration according to (—) Vinal and Craig [9], and (▽) Danel and Plichon [10].

The concentration of H_2SO_4 in the pore volume of PAM and AMCL increases. The diffusion of H_2SO_4 out of the plate is a slow process and depends on the organisation of the pore system. Vinal and Craig [9], and Danel and Plichon [10] have established that the solubility of $PbSO_4$ depends on H_2SO_4 concentration. Fig. 15 shows that on increase of $C_{H_2SO_4}$ from 1.12 to 1.30 s g, the solubility of $PbSO_4$ decreases five times. It can be expected that during charging, the H_2SO_4 solution will be most concentrated in the pores of the AMCL and in the inner parts of PAM. Hence, the solubility of $PbSO_4$ will be low there. In the above mentioned plate layers, the rate of $PbSO_4$ oxidation will slow down with increase of the H_2SO_4 concentration. Some $PbSO_4$ crystals will remain unoxidised in the charged plate. Fig. 14 illustrates the distribution of these unoxidised $PbSO_4$ crystals in the interior of the charged plate. Fig. 13 shows that after 380 cycles, the quantity of large pores is small. Hence, the diffusion flows of H_2SO_4 from the interior of the plate towards the bulk solution are strongly impeded. The charge efficiency in the plate interior declines.

The concentration of H_2SO_4 in the pores of PAM should be kept as low as possible on charge. This can be done by facilitating the transport of H_2SO_4 from the plate interior to the bulk of the solution, which can be achieved through creating an appropriate pore system in the PAM. The $PbSO_4$ solubility can also be affected through the formation of Pb^{2+} complex ions whose solubility should not depend on the concentration of H_2SO_4. The density of PAM as well as the volume and concentration of H_2SO_4 in the cell also affect the processes of residual sulphation of the plate interior. Many desulphation additives have appeared in the market recently. The advertisements claim that they extend battery life and power output. The efficiency of these additives will depend on their influence on the solubility of $PbSO_4$ (through complex formation) at increased $C_{H_2SO_4}$ as well as on their effect (positive or negative) on the structure of PAM.

3.5.4. Dependence of the size of β-PbO_2 crystals as a function of their distance from the spine surface

From the half-width of the characteristic diffraction peaks it is possible to calculate the size of the β-PbO_2 crystals. Fig. 16 illustrates the changes in the average β-PbO_2 crystal size at various distances from the spine surface. The half-widths of the diffraction peaks corresponding to interfacial distances 0.350 nm of the crystal lattice of β-PbO_2 were used for the calculating the sizes of β-PbO_2 crystals. The latter are between 34 and 42 nm. It can be seen that the closer the β-PbO_2 crystals are to the spine surface, the smaller their size. This phenomenon is related to the effect of H_2SO_4 concentration (pH of the solution) on the crystallisation processes of β-PbO_2.

3.5.5. Distribution of PAM phase composition along the height of the SGTP plate

Fig. 17 presents X-ray patterns for samples of the soft PAM (PAM and AMCL layers are not clearly differentiated) taken from the uppermost and from the bottom parts of the tube. The sample from the upper part of the tube features a characteristic peak for β-PbO_2 with a height of the order of 1900–2100 cps and there is no indication of the presence of other crystal phases. In the bottom part of the tube, the height of these peaks is 4700–5000 cps and the PAM contains considerable amounts of $PbSO_4$ and small amounts of α-PbO_2 (and/or tetragonal-PbO). This change in the composition with tube height is a clear indication of electrolyte stratification.

Cycling was conducted at 18% overcharge ($F_{ch} = 1.18$). At this high charge factor, even intense gas evolution cannot prevent the stratification of electrolyte in the AGM separator.

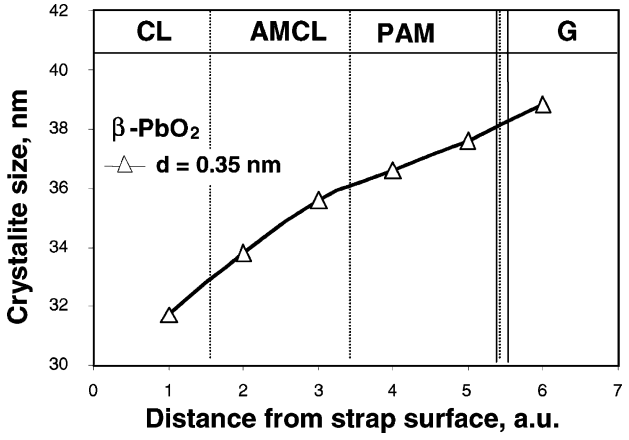

Fig. 16. Changes in β-PbO_2 crystal size as a function of distance from the strap surface.

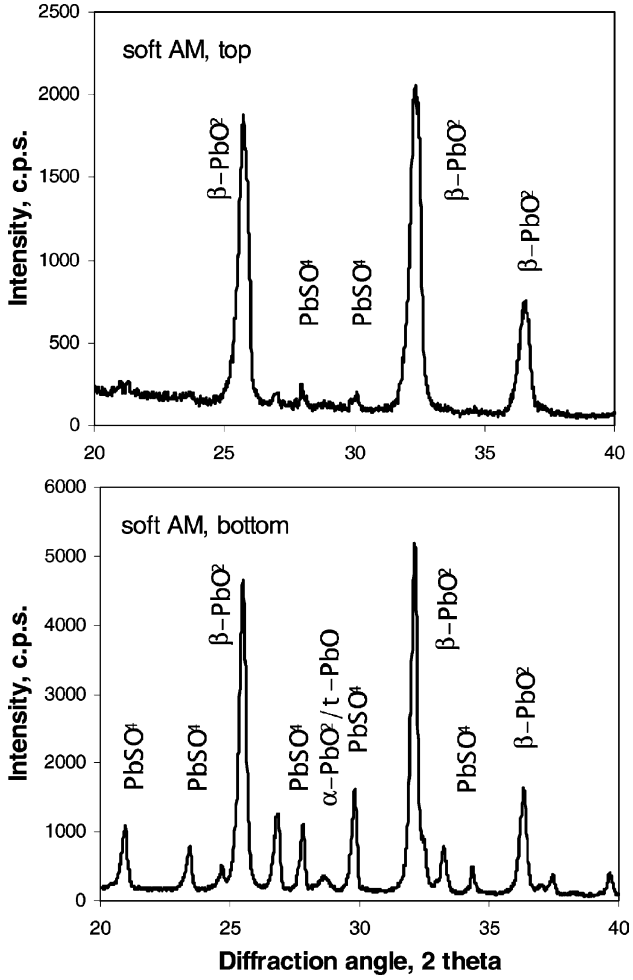

Fig. 17. X-ray patterns for samples of soft PAM taken from the top and bottom parts of a plate.

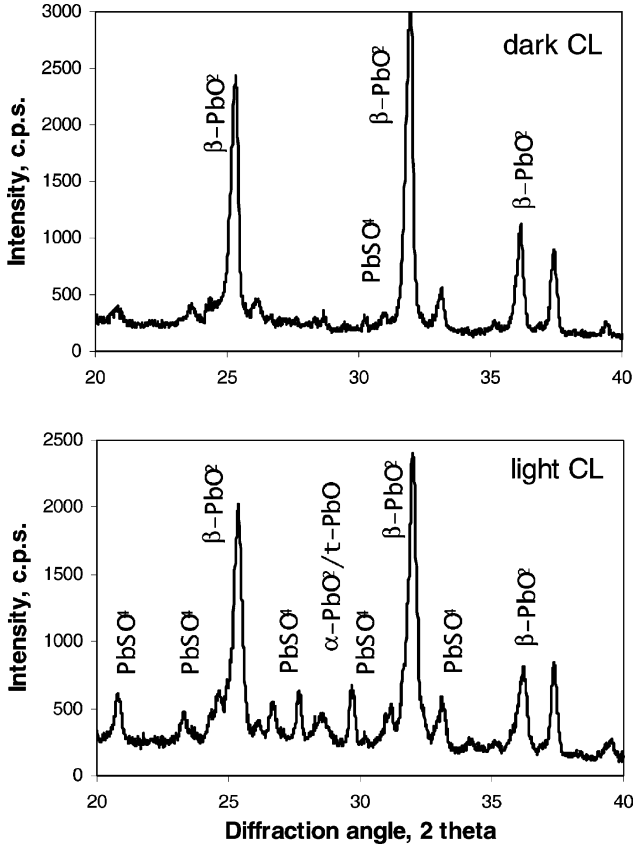

Fig. 18. X-ray patterns for the dark and light brown zones of the corrosion layer.

Finally, the phase composition of the corrosion layer formed on the strap surface was investigated. The PAM layer was stripped off leaving only the corrosion layer, which featured dark brown and light brown zones. Fig. 18 presents the X-ray patterns for the two types of zones.

The dark brown zone of CL is observed in the upper part of the plate. The light brown one is in the bottom part. While the dark brown zones contain negligible amounts of $PbSO_4$ and α-PbO_2 the latter's content in the light brown zones of the CL are much greater. The lighter zones contain less β-PbO_2 than the dark brown ones. This shows that the CL is less conductive in the bottom part of the plate than in its upper part.

It is questionable whether the electrolyte stratification is a result of the lower conductivity of the CL in the bottom part of the plate which does not allow this part to charge fully or vice versa, the stratification is responsible for the incomplete charge of the bottom part of the CL. Obviously, the dependence of $PbSO_4$ crystal solubility on H_2SO_4 concentration plays an important role in formation of light brown zones, too.

3.5.6. Evolution of the structure of the PAM and of the interface PAM/strap grid on cycling

These structural changes were followed through scanning electron microscopy.

3.5.6.1. Immediately after formation (first cycle). Fig. 19a illustrates the PAM macrostructure. The latter comprises a skeleton built up of PbO_2 aggregates some of which have preserved the matrix of 4BS crystals. These aggregates are sized between 6 and 10 μm, which indicates that some of the 4BS crystals have partially dissolved in the suspension. Fig. 19b presents the microstructure of the PAM. It consists of agglomerates of coalesced lead dioxide particles, rounded in shape, and needle-like particles.

Fig. 19c shows the macrostructure of the corrosion layer obtained during the formation process. The microstructure features tightly interconnected PbO_2 particles forming a smooth surface.

3.5.6.2. After 100 cycles. Fig. 20a and b presents SEM micrographs of the macrostructure of PAM.

Some differences are observed between the PAM structure on the side of the solution (Fig. 20a) and that on the side of the CL (Fig. 20b). On comparing Fig. 19a with Fig. 20a and b it can be noticed that the macrostructure of PAM has

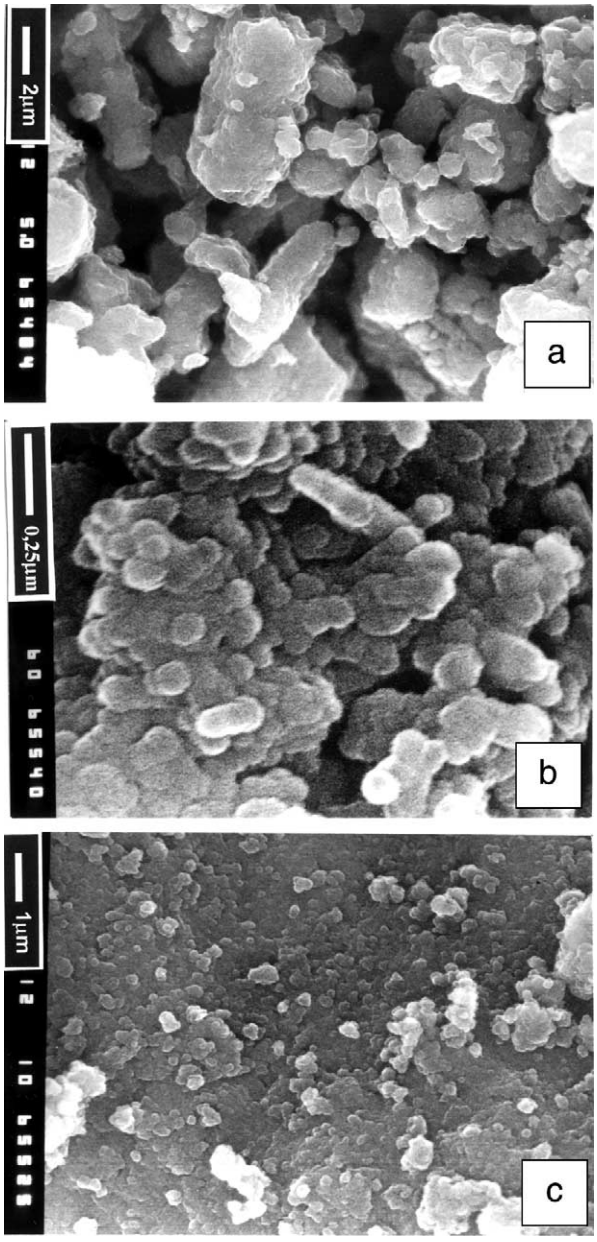

Fig. 19. (a) Macrostructure (aggregates and skeleton) of PAM; (b) microstructure (agglomerates and particles) of PAM obtained after formation; (c) structure of the corrosion layer formed on the strap surface during formation.

undergone serious changes for 100 cycles: the aggregates with the shape of 4BS crystals have disappeared and the PAM has transformed into a spongy mass with large pores in the PAM layer near the CL.

Fig. 20c and d shows the structure of a PAM sample with a pronounced hardness. It consists of spherical or needle-like particles (Fig. 20d), which have adhered tightly to one another. Sporadic micropores are observed here and there (Fig. 20d). Such a membrane structure implies that it will be difficult for the ion flows to penetrate into the interior of the agglomerate and hence the utilisation of PAM will be reduced [11].

Fig. 21a and b shows SEM micrographs of the structure of the inner PAM layers, adjacent to the CL. Though the cell was fully charged, a considerable amount of $PbSO_4$ crystals have remained unoxidised to PbO_2 (i.e. residual sulphation). The distribution of the rate of $PbSO_4$ oxidation in the cross section of the plate was discussed before (Fig. 14). Fig. 21b shows that $PbSO_4$ crystals are partly dissolved in the inner parts of the plate, which supports the above discussed phenomena of residual sulphation that influence the charge efficiency of the plate. When these residual $PbSO_4$ crystals are in the AMCL layer, their effect on the capacity is stronger.

3.5.6.3. After 200 cycles. On autopsy of the strap grid tubular plates after 200 cycles, two layers were distinguished in PAM. These layers are presented diagrammatically in Fig. 22.

The corrosion layer is mostly a dense non-porous mass, brown in colour, with sporadic cracks here and there. A ‘‘shell’’ of PAM is separated easily from the interface and a thin brittle AMCL layer is distinguished between this shell and the CL. The functions of this AMCL were identified in [3]. In the present case of battery cycling according to the ECE-15 test profile, the structure of this AMCL layer differs notably from that of the PAM and of the CL. Two types of structures are observed in the AMCL: the first is a fairly powdery and highly porous structure with loose contact between the agglomerates, and the second one is a compact (dense) structure built up of thick (several microns) aggregates with smooth surface similar to the one presented in Fig. 20b. Residual $PbSO_4$ crystals are found in both AMCL structures of the fully charged plate. It can be expected that the powdery structure would often lose contact with the PAM layer. Consequently, parts of the PAM would be excluded from the current generation and accumulation processes and the capacity of the plate would decrease. The second type AMCL structure is compact and carries the electric current between the strap and the PAM. The ratio between these two types of structure may determine the power output of the cell. Besides this distribution of active mass layers through the cross-section of the tubes, a certain distribution of the PAM density along the height of the tubes was also observed. There were hard PAM zones and soft ones.

3.5.6.4. After 380 cycles. The plate tubes were cut open and removed. Part of the PAM fell down in the form of small pieces. Another part came apart as a shell and a third part of PAM remained connected to the strap. No cracks were observed in the straps due to corrosion. No active mass leaking out of the tubes was detected either.

Three types of macrostructures were observed in the PAM and AMCL:

- Skeleton with aggregates of greater individuality and highly porous microstructure (Fig. 23a). This structure provides a large surface for the electrochemical reaction

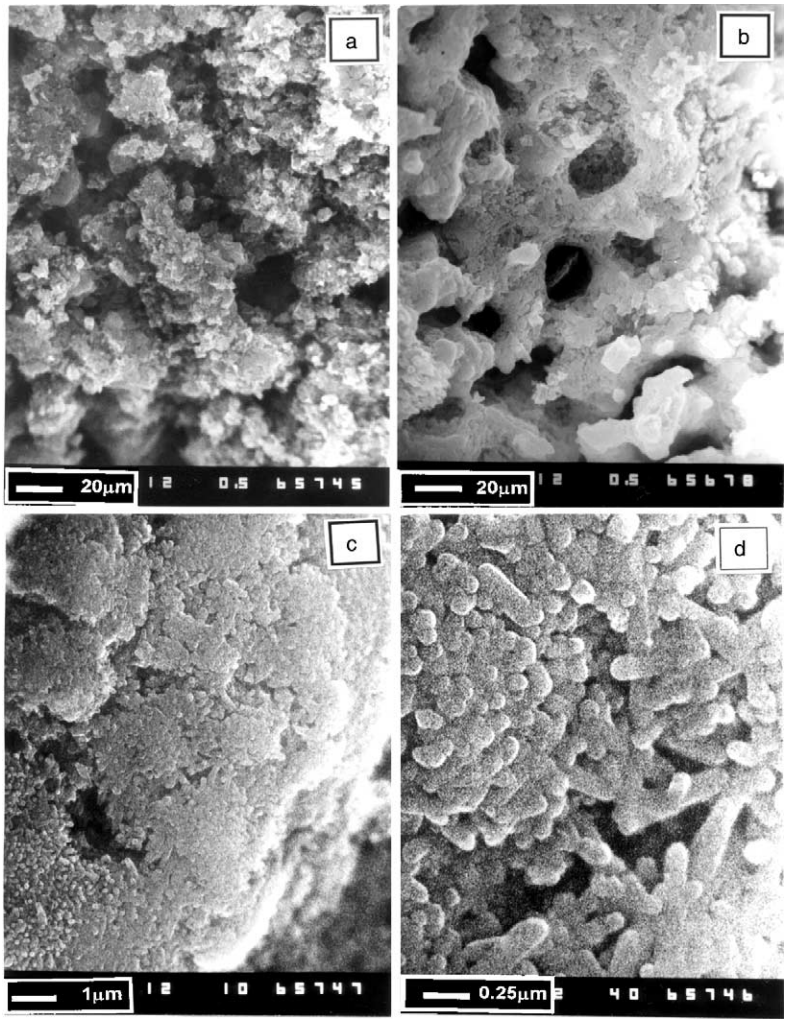

Fig. 20. Macrostructure of: (a) the PAM layer facing the solution, and (b) the PAM layer facing the CL, after 100 cycles; (c and d) microstructure of the PbO_2 samples taken from the hard PAM zones.

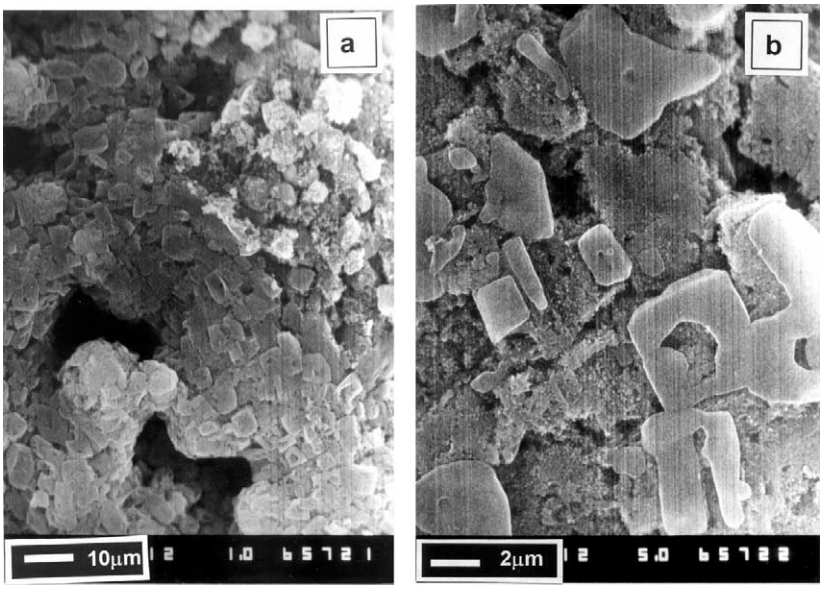

Fig. 21. Macrostructure of the PAM layer facing the CL after 100 cycles.

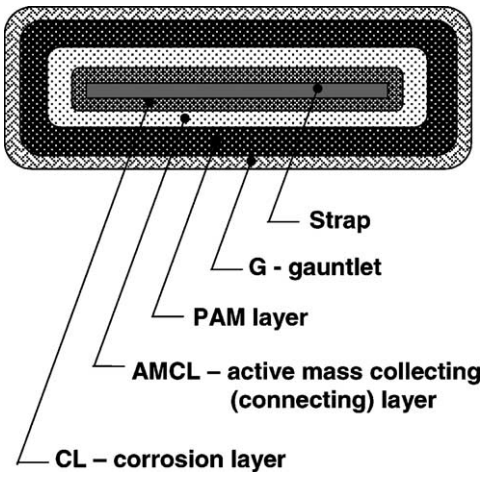

Fig. 22. Schematic representation of the active mass layer through the cross-section of the tube after cycling.

to proceed and also a well developed pore system allowing easy transport of the ion, H_2O and H_2SO_4 flows. The only limitation with this type of macrostructure is that when the contact surface between the aggregates and agglomerates decreases during discharge, the ohmic resistance will increase and hence may limit the utilisation of the PAM. Besides, this type of structure is mechanically less stable and disintegrates if it is not supported by the tube. Thanks to the mechanical support provided by the tubes these plates have a cycle life much longer than that of pasted plates.

- The second type of PAM structure is hard and is presented in Fig. 23b. The SEM micrographs of the skeleton structure feature low microporosity ($r < 0.1$ μm) and skeleton surface with membrane properties. Such a membrane structure was established earlier [11]. It impedes the access of H_2SO_4 into the volume of the aggregates and

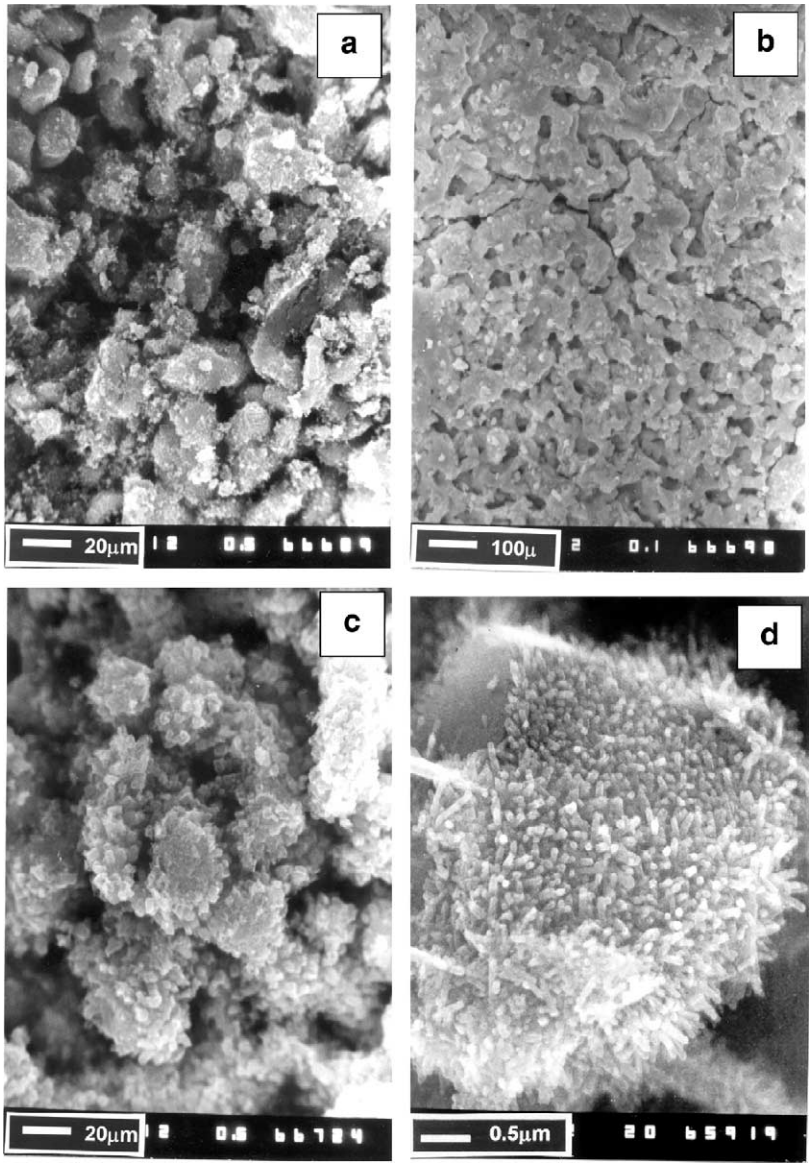

Fig. 23. Three types of macrostructures are formed during the first 380 cycles (ECE-15 test): (a) soft; (b) hard; (c and d) sulphated.

$Pb(OH)_2$ and PbO are formed there [12]. Consequently, the utilisation of PAM decreases. Moreover, internal stresses are created in the skeleton, which cause its branches to crack.

- Fig. 23c and d shows pictures of the third type of skeleton structure that features aggregates covered with small $PbSO_4$ particles. Probably, these are residual $PbSO_4$ crystals, which remain unoxidised for many cycles. At higher magnifications (Fig. 23d) it can be seen that there is a ''carpet'' of needle-like PbO_2 particles covering the surface of the $PbSO_4$ crystals. These residual $PbSO_4$ crystals differ in shape as compared to the unoxidised (residual) $PbSO_4$ crystals in the charged plate presented in Fig. 21. The shape of a PbO_2 aggregate or of an unoxidised $PbSO_4$ crystal depends on the diffusion path of Pb^{2+} ions before they are oxidised [13]. In the structure presented in Fig. 23, the diffusion path of Pb^{2+} ions is short and Pb^{2+} ions are oxidised in the PbO_2 layer covering the $PbSO_4$ crystal surface. In the structure shown in Fig. 21, the diffusion path of Pb^{2+} ions is long. The obtained PbO_2 aggregate does not ''remember'' the original $PbSO_4$ crystal that has been oxidised.

3.5.6.5. After 600 cycles. On cutting the tubes open, part of the PAM disintegrated into powder and another part formed a shell (i.e. hard zones), which detached from the straps because the AMCL was fairly brittle. The brittle zones of PAM + AMCL were a bit larger than those in the plates that had undergone 380 cycles.

The PAM and AMCL are composed of zones with dimensions ranging between 200 and 500 μm. Two types of zones were observed: some of them were highly porous, similar to the structure presented in Fig. 23a and c and others had smooth surface, similar to the one given in Fig. 23b.

3.5.6.6. After 1000 cycles. After 1000 cycles the PAM and AMCL structures were very similar to those of the PAM at the 600th cycle but some of the straps were broken by intergranular corrosion. This was one of the life limiting parameters. The tubes had soft and hard zones on touching. Disintegration of the skeleton structure to powder was established in the soft zones. This was the second reason for the decline in battery power output. It is a challenge to discover the mechanism of the degradation of the PAM macrostructure and to find methods to restore this structure after the softening. This would be possible as the tubes maintain the volume of PAM unchanged and the pore volume (0.17 cm^3/g PAM) is below the critical pore volume (0.28 cm^3/g PAM) above which the PAM disintegrates irreversibly. It is necessary to discover the driving forces responsible for the degradation of the PAM skeleton and to elaborate charging algorithms that could suppress these forces. Thus, the cycle life of the battery could be prolonged substantially.

4. Conclusions

1. Flattened elliptic or rectangular tubular plates (3 and 5 mm thick) with strap grids have been developed based on the die-cut or cast grid technologies. This novel plate design yields capacity and power performance similar to that of pasted plates and cycle life close to that of tubular batteries. The low value of the γ-coefficient for these plates ensures higher power output of the batteries on discharge, which makes them suitable for EV applications. Through confining the PAM with in the tubes and thus keeping its volume constant, the cycle life of the batteries is improved substantially as compared to that of traction batteries with pasted plates.
2. It has been established that the cycle life of VRLA batteries with SGTP plates depends on the value of the initial charge current I_1, on the $I_1U_2I_3$ charging algorithm, and on the charge factor F_{ch}. There are optimum values for the above parameters, which ensure maximum battery cycle life performance. For SGTP batteries a charge algorithm $I_1 \approx 1.5C_5$ A, $U_2 = 15.2$ V, $I_3 = 0.05C_5\,A$ and $F_{ch} \approx 118\%$ yields a cycle life of 6000 ECE-HEV cycles. This high overcharge, however, increases the water loss and hence watering of the batteries is needed.
3. During cycling both PAM and AMCL disintegrate through the following mechanisms:
   (a) When the PAM and the AMCL are built up of globules tightly adhering to each other, the aggregates' surface has membrane properties. It impedes the transfer of H_2SO_4 into the volume of the aggregates and thus decreases the available quantity of PAM which is involved in the reactions. Consequently, the capacity declines.
   (b) When the PAM and the AMCL are built up of individual agglomerates with micropores in between, a porous mass is formed. When the apparent density of this porous mass decreases, the contact between the individual agglomerates is strongly impaired and the active mass disintegrates into powder. The tubes suppress these phenomena and prolong the cycle life.
   (c) During discharge, the H_2SO_4 concentration increases in the pores of the inner plate parts close to the straps. The solubility of the $PbSO_4$ crystals depends on the H_2SO_4 concentration. It is low in concentrated H_2SO_4 solutions and high in diluted ones. In the pores of AMCL, the H_2SO_4 concentration is high and the solubility of $PbSO_4$ crystals is low. Parts of the $PbSO_4$ crystals remain unoxidised in the PAM of the charged plates. Consequently, the capacity of the plate is low. The effect of residual sulphation of the positive plate is stronger when these phenomena occur in the AMCL layer. The residual sulphation depends on the pore system of

PAM, the PAM density, the volume and concentration of H_2SO_4 in the cell as well as on the additives to the electrolyte.

4. The present investigation has established that SGTP batteries with 5 mm plate thickness can endure 5500 cycles (55,000 km) when tested according to the ECE-HEV cycling test protocol. If the test protocol ECE-15 is employed, the SGTP batteries have a life of about 1000 cycles. This cycle life corresponds to about 50,000 km mileage. It has been established that photovoltaic SGTP batteries (3 mm thick plates) have a cycle life longer than eight gross cycles corresponding to more than 8800 h of cycling.

Acknowledgements

The research team of CLEPS wants to sincerely thank the European Community, INCO and ALABC/EALABC for their financial support for the electric vehicle part of this investigation performed within the Brite-Euram Project BE97-Y085 and to the European Commission for the financial support for the photovoltaic part of the research (ABLE project). We want to extend our special thanks to Dr. A. Cooper for his valuable help as supervisor of the Brite-Euram Project.

References

[1] D. Pavlov, E. Bashtavelova, J. Electrochem. Soc. 133 (1986) 241.
[2] K. Takahashi, M. Tsubota, K. Yonezu, K. Aldo, J. Electrochem. Soc. 130 (1986) 2144.
[3] D. Pavlov, J. Power Sources 53 (1995) 9.
[4] International standard IEC 61427 (1997).
[5] Specification of test procedures for electric vehicle traction batteries, EUCAR, December 1996.
[6] Specification of test procedures for hybrid electric vehicle traction batteries, EUCAR, October 1997.
[7] D. Pavlov, A. Dakhouche, T. Rogachev, J. Power Sources 42 (1993) 71.
[8] D. Pavlov, I. Balkanov, J. Electrochem. Soc. 139 (1992) 1830.
[9] G.W. Vinal, D.N. Craig, J. Res. Natl. Bur. Stand. 22 (1939) 55.
[10] V. Danel, V. Plichon, Electrochim. Acta 27 (1984) 1643.
[11] M. Dimitrov, D. Pavlov, J. Power Sources 93 (2001) 234.
[12] D. Pavlov, I. Balkanov, P. Rachev, J. Electrochem. Soc. 134 (1987) 2390.
[13] D. Pavlov, E. Bashtavelova, D. Simonsson, F. Ekdunge, J. Power Sources 30 (1990) 77.